Cascaded Indoor Flight Controller Design for a Miniaturized Tiltwing Aircraft

J. Müller*, D. Schatten, D.F. Duda, and D. Moormann
RWTH Aachen University, Templergraben 55, 52062 Aachen Germany

ABSTRACT

This paper presents a concept for indoor operation of a tiltwing aircraft based on a cascaded controller for translational velocity commands. We outline the challenges of flying a tiltwing aircraft indoors, especially with regard to navigation and confined space requirements. By using Incremental Nonlinear Dynamic Inversion (INDI), we are able to control our micro tiltwing aircraft in translational direction with respect to a horizontal reference frame. Here, focus is placed on modeling the translational control effectivities considering aerodynamic and propulsion models. The control performance is analyzed by means of simulation.

1 INTRODUCTION

Operating unmanned aerial systems in confined spaces, including indoor settings, offers a number of opportunities, including remote aerial surveillance, inspections, and data collection. However, such an operation environment involves various challenges, especially when using tiltwing aircrafts. These hybrid, unmanned vehicle have the ability to vertically take off and land (VTOL) and also fly in a fast, efficient forward flight. Accordingly, these systems require different airspace dimensions for safe operation, depending on the desired airspeed.

In this paper, we present a concept for controlling a miniaturized tiltwing aircraft for indoor operations. Initially, a dynamic aircraft model, conceptional constraints for controlling a tiltwing aircraft in confined spaces and the indoor position and heading determination are presented. Afterwards, the translational controller implementation is introduced with focus on the application of the INDI control law on the aircraft's translational motion. Since the examined aircraft naturally rotates its wing and operates in a low Reynolds number range, instationary effects occur, especially during the transition from thrust- to wing-borne flight. This leads to challenges in creating an aerodynamic model of the aircraft, which is required for the controller design. We address this issue by using a translational INDI controller, which, due to its robustness, allows for simplified aerodynamic modeling and compensates for model inaccuracies. The modeling of this control concept is described in Section 3, along with other required controller cascade. Simulation results for the implemented controller are presented in Section 4 and a conclusion is drawn in Section 5.

*Email address: julian.mueller@fsd.rwth-aachen.de

2 INDOOR FLIGHT

The tiltwing aircraft on which this study is based is shown in Figure 1 and is further referred to as *Idefix*. With a span of $b = 0.5\,\mathrm{m}$ and a mass of $m = 175\,\mathrm{g}$, it was especially designed for indoor operations.

Figure 1: The tiltwing aircraft *Idefix*

The control devices of *Idefix* are shown in Figure 2. In thrust-borne configuration, the main motors positioned at the wing provide lift and roll control, while a tail-mounted motor is used for pitch control and yaw control is provided by aileron deflections.

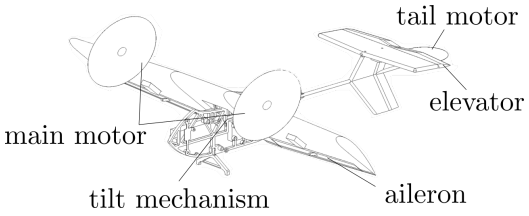

Figure 2: Control devices of the tiltwing aircraft.

With increasing longitudinal velocity, the aircraft continuously transitions from thrust- to wing-borne flight, and the main wing rotates along the lateral axis. This process is further referred to as *transition*. In wing-borne configuration, the tiltwing aircraft is actuated like a conventional aircraft except for the yaw-control, which mainly originates from differential thrust instead of a rudder.

2.1 Dynamic model description

The aircraft's translational motion is described by following equation:

$$\begin{bmatrix} \dot{u} \\ \dot{v} \\ \dot{w} \end{bmatrix} = \begin{bmatrix} \dot{u}_F \\ \dot{v}_F \\ \dot{w}_F \end{bmatrix} + \begin{bmatrix} p \\ q \\ r \end{bmatrix} \times \begin{bmatrix} u \\ v \\ w \end{bmatrix} \tag{1}$$

Here, $[u\ v\ w]^T$ describes the translational velocity and $[p\ q\ r]^T$ the rotational velocity in body fixed coordinates, see Figure 3. The term $[\dot{u}_F\ \dot{v}_F\ \dot{w}_F]^T$ considers the acceleration resulting from external forces acting on the aircraft's center of gravity. As shown in Figure 3, these forces include the thrust force $\vec{T}$, which is aligned with the wing-chord and tilted by σ towards the aircraft's longitudinal axis, the aerodynamic force $\vec{A}$ resulting from the airspeed and the gravitational force $\vec{G}$. Equation 2 represents these forces in body-fixed coordinates.

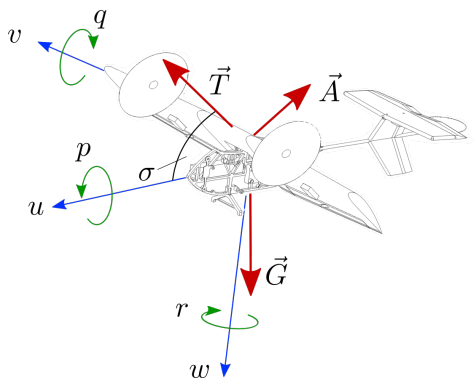

Figure 3: Direction of body fixed translational, angular velocities and acting forces.

$$\begin{bmatrix} \dot{u}_F \\ \dot{v}_F \\ \dot{w}_F \end{bmatrix} = \begin{bmatrix} \frac{T \cdot cos(\sigma)}{m} - \frac{G}{m} \cdot sin(\Phi) - \frac{A_x}{m} \\ \frac{G}{m} \cdot cos(\Theta) \cdot sin(\Phi) - \frac{A_y}{m} \\ \frac{-T \cdot sin(\sigma)}{m} - g \cdot cos\Phi \cdot cos(\Theta) - \frac{A_z}{m} \end{bmatrix} \tag{2}$$

The angular motion is described in Equation 3 with $[\dot{p}\ \dot{q}\ \dot{r}]^T$ being the body-fixed rotational accelerations, I representing the inertia tensor, and $[M_x\ M_y\ M_z]$ covering all external moments such those generated by the motors or the deflection of the aerodynamic control surfaces.

$$\begin{bmatrix} \dot{p} \\ \dot{q} \\ \dot{r} \end{bmatrix} = I^{-1} \left[\begin{bmatrix} M_x \\ M_y \\ M_z \end{bmatrix} - \begin{bmatrix} p \\ q \\ r \end{bmatrix} \times \left(I \cdot \begin{bmatrix} p \\ q \\ r \end{bmatrix} \right) \right] \tag{3}$$

For simulations, the aerodynamic forces and moments are modeled using an element-based approach. Structural parts, such as the wing, control surfaces and fuselage are subdivided into sections with associated drag and lift polars. The associated forces and moments can be derived by calculating the inflow at each element. For elements exposed to inflows with an angle of attack $\alpha > 12\,^\circ$, the aerodynamic polars are extrapolated according to [1]. Each element's associated aerodynamic forces and moments are then superimposed in the aircraft's center of gravity [2]. Flight tests with various tiltwing aircraft have shown that the described approach models the aerodynamics with sufficient accuracy.

2.2 Transition flight in confined space

Flight systems are restricted by specific translational acceleration and deceleration limits, as well as by certain flight attitudes in order to operate safely. These aircraft-specific limitations directly affect the required flight space for defined maneuvers. Thus, the proximity to obstacles, such as walls and ceiling, pose significant limitations that must be considered in mission planning and controller architecture for autonomous indoor operation. Unlike thrust-borne multi-copters, which have similar limitations in all directions, a transition-capable aerial system like *Idefix* has direction-specific limitations that pose a special challenge in controlling these vehicles.

As shown in Figure 4, tiltwing aircrafts accelerate continuously along the body-fixed longitudinal axis, building up a desired airspeed while tilting the wing downward to the fixed-wing position. In the process, the airspeed increases, allowing the wing to generate more lift. To maintain altitude, the weight force must be in balance with the lift and thrust forces. In doing so, the controller must account for nonlinear limitations of the flight system, such as aerodynamic stall. In contrast to the transition of tiltwing aircrafts in outdoor operations, the influence of wind can be neglected indoors. This allows to estimate the aerodynamic inflow only based on the direction of translational motion and the attitude angles of the aircraft. In addition to these aerodynamic limitations, the absolute deflection of the actuators, such as the elevators and ailerons and the thrust magnitude from the propellers, are limited. Alongside these static limitations, the actuators are subjected to dynamic limitations, including the angular velocity of the tilt mechanism. As some of these actuators act only in specific directions, these limitations are directional-dependent.

To approximate the required transition length along a straight line, a constant translational acceleration of $\dot{u} = 1\,\mathrm{m/s^2}$ is assumed. Simulations show, that for *Idefix* a sufficient wing-borne airspeed is reached at $u = 7\,\mathrm{m/s}$. Using these boundary conditions, the double integration of

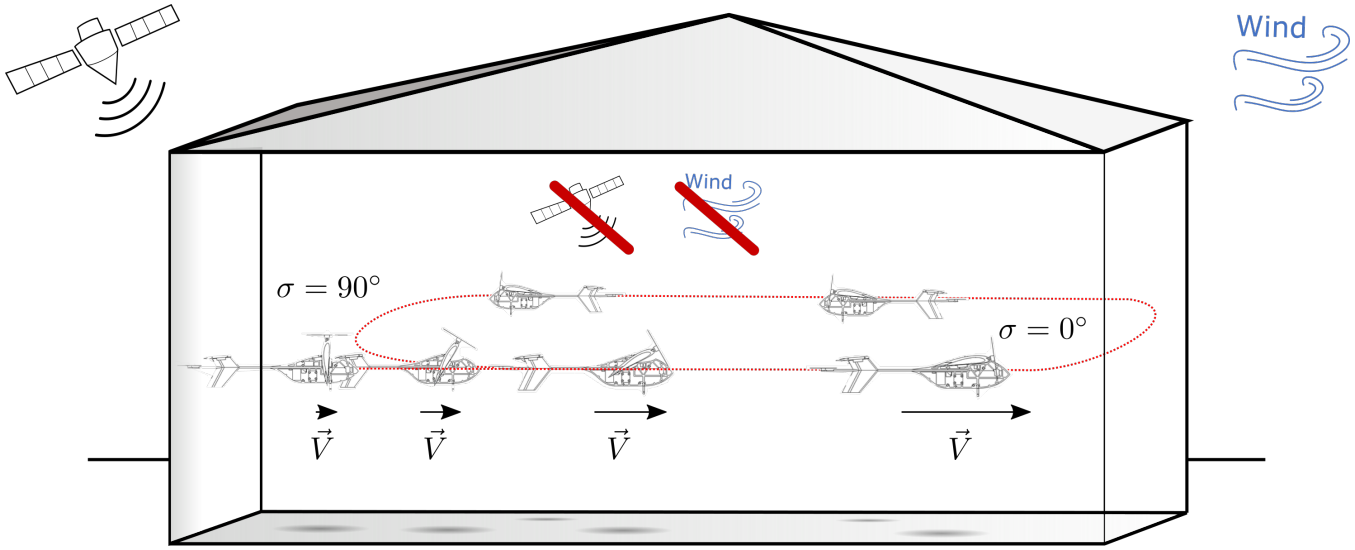

Figure 4: Indoor transition from thrust- to wing-borne flight

Equation 1 yields a transition length of $l_{tr} \approx 25\,\mathrm{m}$. Thus, to fully transition from thrust-borne to wing-borne flight and back with $\dot{u} = \pm 1\,\mathrm{m/s^2}$, a minimum room length of $l \approx 50\,\mathrm{m}$ is required. This considerably restricts the range of indoor operation for these tiltwing system.

To allow for wing-borne operation in smaller areas, the space requirement for transitions along a circular path is evaluated. Assuming no external disturbance, such as no prevailing wind, the minimum curve radius R_{min} can be calculated depending on the horizontal ground speed V_k and lateral acceleration a_y, which during turns is dependent on the aircraft's roll angle [3]. With Equation 4 and Equation 5, the minimum curve radius for wing-borne flight can be determined to $R_{min} = 7.5\,\mathrm{m}$.

$$R_{min} = \frac{V_k^2}{|a_y|} \tag{4}$$

$$a_y = tan(\phi) \cdot g \tag{5}$$

This presumes a maximum roll angle of $\phi = 45\,°$ and an increased ground speed of $v = 8.5\,\mathrm{m/s}$, which accounts for the extra lift required during turns. Including a safety margin of $1\,\mathrm{m}$ to each side, this results in a minimum required room size of $17\mathrm{x}17\,\mathrm{m}$ for continuous circular wing-borne flight, which is about three times less than for a unidirectional transition. If the available room size is smaller than that, the maximum allowed velocity must be reduced accordingly, resulting in a combination of thrust- and wing-borne flight.

2.3 Indoor position and heading determination

The main application for *Idefix* is autonomous indoor flight. Flying inside enclosed rooms leads to different problems for the navigation solution than flying outdoors. While GNSS systems are usually used to determine the position outside buildings, they are often unavailable indoors. Also the orientation along the earth's magnetic field is also only possible to a limited extend, since the magnetic field can be strongly disturbed by building structures or electric components. To provide a reliable navigation solution, alternative approaches can be used, for example camera-based [4], ultra-wide-band (UWB) [5] or ultrasound based positioning systems (USP) [6]. The applicability of these systems mostly depends on the aircraft and the accompanied requirements such as accuracy, update rate, weight, range, latency and size.

For the tracking of *Idefix* we employ the ultrasound-based positioning system *Marvelmind* [6]. This multilateration system estimates the aircraft's position by measuring the run time of the ultrasound signal using stationary and mobile beacons, see Figure 5.

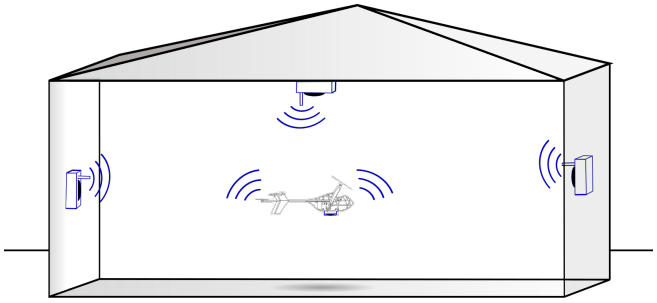

Figure 5: Architecture of the USP-System *Marvelmind*

By attaching two mobile beacons with known spacing to *Idefix*, the aircraft's heading can also be estimated from the beacon's relative position vector. The system specifications of *Marvelmind* are listed in Table 2.3. Using an extended Kalman filter [7], the position measurements are fused with the onboard inertial measurement unit (IMU) data to improve the position and heading estimation. The estimation uncertainties resulting from the measurement behavior of the USP are also considered in the simulation.

mass mobile beacon	6.5 g
size mobile beacon	30 x 30 x 20 mm
position deviation	±20 mm
update rate	8 Hz
latency	0.125 s
range	30 m

Table 1: Specifications of the USP system "Marvelmind" [6]

3 CONTROLLER IMPLEMENTATION

Idefix's flight controller runs with a sample time of $T = 0.05\,\mathrm{s}$ and is divided into following cascades: guidance, translational and attitude controller, see Figure 6. In the following section, these cascades are presented with focus on the translational controller.

3.1 Guidance Controller

Since the translational cascade only controls translational accelerations, a super-ordinate guidance controller is necessary. For testing and validation purposes, we use a horizontally and vertically saturated proportional derivative speed controller, enabling straight flight in horizontal x_h-, y_h- and z_h-direction. Control deviations on velocity level are projected onto the commanded accelerations $\vec{a}_c$. Gains for the guidance controller were determined iteratively by simulations to allow for minimum overshoot.

3.2 Translational Controller

The aircraft's capability to transition from vertical thrust-borne flight to horizontal wing-borne flight is accompanied by a complex non-linear characteristics of the translational motion. Extensive knowledge of the flight system's aerodynamics in all flight states is typically required to control this motion. However, small tiltwing aircrafts, such as *Idefix*, operate in a low Reynolds number regime of $0 < \mathrm{Re} < 70000$. Element-based models, which are used for conventional controller design, come with significant uncertainties [8, 9]. Therefore, a translational controller based on the concept of INDI is applied for *Idefix*, allowing for robust control with lower requirements on the aircraft model accuracy [10, 11].

When INDI is applied to the translational motion of *Idefix*, the roll angle, pitch angle, specific thrust $t_m = T_m/m$ and tilt angle of the wing are identified as control variable vector $\vec{u} = [\phi, \theta, t_m, \sigma]^T$. The corresponding control law is given in Equation 6, which calculates the control variable vector u based on the control difference between the commanded acceleration $\vec{a}_c$ and the aircrafts translational acceleration $\vec{a}$ [11].

$$\vec{u} = \vec{u}_f + B^{-1}(\vec{a}_c - \vec{a}) \tag{6}$$

Equation 6 can also be reformulated in incremental form, see Equation 7. This reformulation yields the change in the control variables, depending on the inverse of the control effectivity matrix B and the commanded deviation from the controlled state.

$$\Delta\vec{u} = \vec{u} - \vec{u}_f = B^{-1}(\vec{a}_c - \vec{a}) \tag{7}$$

The control effectivity matrix B is derived from a systems linearization and describes the change in acceleration caused by a change in control variables. This matrix strongly depends on the current state of the control variables, leading to complex interrelations between them. In contrast to the rotational INDI, translational accelerations a are measured directly and do not need to be derived from velocity

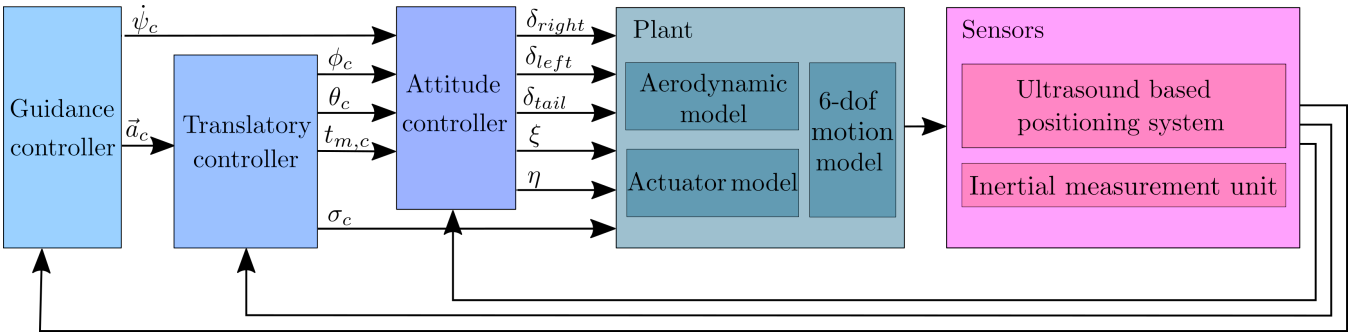

Figure 6: Controller Architecture

measurements. This is also true for the feedback of the control variables ϕ and θ which are direct outputs from the navigation solution. However the control variables t_m and σ are yet to be estimated by dynamic models analogous to the rotational INDI [12].

Coordinate Systems

Choosing coordinate systems and rotation orders of the attitude angles that do not show any singularities in the attitude's description within the entire flight envelope is necessary to describe the control effectivities. Following, the required coordinate systems are presented.

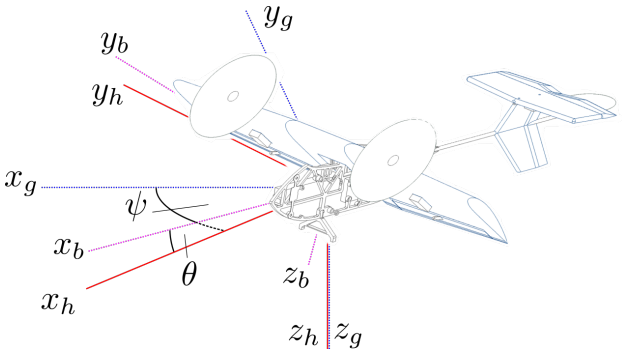

Figure 7: Geodetic, horizontal and body-fixed coordinate system

Figure 7 illustrates the horizontal coordinate system indexed $\square_h$ along with the body-fixed coordinate system indexed $\square_b$ and geodetic coordinate system indexed $\square_g$. In the horizontal coordinate system x_h corresponds to the projection of the body fixed axis x_b onto the x_g-y_g-plane. The z_h-axis is equivalent to the z_g-axis and the y_h-axis lies in the horizontal plane with its direction resulting from the convention of a right turning coordinate system. This allows for formulating the aircraft's attitude with respect to the horizontal frame according the standard rotation order ψ, θ, ϕ with $\psi = 0$.

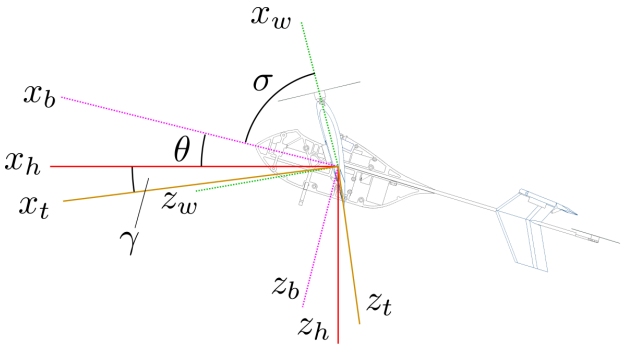

Figure 8: Trajectory, horizontal, body- and wing-fixed coordinate system

The wing-fixed coordinate system indexed $\square_w$ is shown in Figure 8. This coordinate system represents the rotation of the body-fixed coordinate system around the y_b-axis about the wing tilt angle σ [12]. Figure 8 also shows the trajectory coordinate system indexed $\square_t$, which is rotated about the slip angle β_f and the slope angle γ with respect to the horizontal coordinate system.

For the translational INDI a reference frame in horizontal coordinates is chosen. All changes in direction and magnitude of the thrust $\vec{T}$, aerodynamic load $\vec{A}$ and weight force $\vec{G}$ due to changes in the control variables are summarized in in the control effectivity matrix B. However, the weight force vector remains unaffected in this reference frame, yielding the zero-entry-matrix $B_{G,h}$. The thrust- and aerodynamic force-related effectivities $B_{T,h}$ and $B_{G,h}$ are more complex and described below.

Thrust control effectivity

Since the tail motor produces less than $10\,\%$ of the main motor thrust and is primarily designated to maintain the pitch equilibrium in thrust-borne and slow forward flight, only the main motor effectivity is considered in the translational control effectivity model. The main motors are aligned with the wing chord and the thrust force can be written as follows:

$$\vec{T}_w = \begin{bmatrix} T_m \\ 0 \\ 0 \end{bmatrix}_w \tag{8}$$

Using a thrust model, the thrust force T_m can be estimated from the current throttle position δ_T and the estimated incident flow velocity. The acceleration in the horizontal frame resulting from this thrust force depends on the aircraft mass m and the current transformation relation $M_{hw} = f(\phi, \theta, \sigma)$.

$$\vec{a}_{T,h} = \frac{1}{m} M_{hw} \vec{T}_w \tag{9}$$

Differentiation of Equation 9 for the control vector $\vec{u} = [\phi, \theta, t_m, \sigma]^T$, allows to derive the corresponding control effectivity $B_{T,h} \in \Re^{3x4}$:

$$B_{T,h} = \frac{d\vec{a}_{T,h}}{d\vec{u}} = \frac{1}{m} \left(\frac{dM_{hw}}{d\vec{u}} \vec{T}_w + M_{hw} \frac{d\vec{T}_w}{d\vec{u}} \right) \tag{10}$$

Appendix A.1 shows the complete derived thrust related effectivity matrix. Due to the transformation relations from the wing coordinate system into horizontal coordinate system, dependencies of the angles ϕ, θ, σ are included in the formulation of $B_{T,h}$. The change of the thrust force magnitude is only dependent on the change of throttle position, and thus the expression $d\vec{T}_w/d\vec{u}$ can written as $[0, 0, dT_m/d\delta_{T_m}, 0]^T$.

Aerodynamic control effectivity

The determination of the acting aerodynamic forces via an aerodynamic model is challenging for *Idefix* because of its highly Reynolds number-dependent lift and drag polars at angles of attack in a range of $-180° < \alpha < 180°$ [9]. Even though models for airfoil lift an drag extrapolation exist in literature [1], they show noticeable uncertainties, especially for $|\alpha| >> 0°$. Alternatively, the aerodynamic forces A_h can be obtained from the force equilibrium in horizontal coordinates according to Equation 11, with $\vec{G}_h$ as the gravitational force, $\vec{T}_h$ as the motor thrust and $\vec{a}_h$ as the aircraft's measured acceleration.

$$\vec{A}_h = \vec{a}_h \cdot m - \vec{G}_h - \vec{T}_h \tag{11}$$

The aerodynamic forces are analyzed in the aerodynamic coordinate system, where they can be divided into lift and drag forces. The aerodynamic force in y_h-direction is assumed to be negligible since only small slip angles are anticipated during both transition and wing-borne flight. Thus, after transforming into the aerodynamic coordinate system with use of the transformation matrix M_{ah}, the aerodynamic force can be written as follows:

$$\vec{A}_a = M_{ah}\vec{A}_h \approx \begin{bmatrix} D \\ 0 \\ L \end{bmatrix}_a \tag{12}$$

The resulting acceleration and the related control effectivity in horizontal coordinates can be described with Equation 13 and 14 with M_{ha} being the transformation matrix from aerodynamic to horizontal coordinate system.

$$\vec{a}_{A,h} = \frac{1}{m} M_{ha}\vec{A}_a \tag{13}$$

$$B_{A,h} = \frac{d\vec{a}_{A,h}}{d\vec{u}} = \frac{1}{m}\left(\frac{dM_{ha}}{d\vec{u}}\vec{A}_a + M_{ha}\frac{d\vec{A}_a}{d\vec{u}}\right) \tag{14}$$

At this point a timescale separation-based assumption affecting the derivatives of the aerodynamic force has to be made. It is assumed, that the aircraft's attitude changes significantly faster than its trajectory. The slope angle γ and the slip angle $\beta_f = \chi - \psi$ of *Idefix* therefore remain constant between two controller time steps. Thus, the transformation matrix M_{ha} can be written as a function of $\phi, \theta, \sigma, \gamma$ and β_f. This also means that the change in the wing's angle of attack α_w is directly influenced by a change in the translational control variables resulting in an analytical description, shown in Appendix A.3. Consequently, Equation 14 can be transformed into Equation 15.

$$B_{A,h} = \frac{d\vec{a}_{A,h}}{d\vec{u}} = \frac{1}{m}\left(\frac{dM_{ha}}{d\vec{u}}\vec{F}_a + M_{ha}\frac{d\vec{F}_a}{d\vec{\alpha}_w}\frac{d\vec{\alpha}_w}{d\vec{u}}\right) \tag{15}$$

Assuming that only the wing induces the aerodynamic force, the derivative $d\vec{F}_a/d\vec{\alpha}_w$ can be expressed with Equation 16 and 17.

$$\frac{\delta L}{\delta \alpha_w} = \frac{\rho}{2}\cdot v^2 \cdot S \cdot C_{L,\alpha_w} \tag{16}$$

$$\frac{\delta D}{\delta \alpha_w} = \frac{\rho}{2}\cdot v^2 \cdot S \cdot C_{D,\alpha_w} \tag{17}$$

These equations includes knowledge of the derivatives of the lift and drag polars with respect to the angle of attack C_{L,α_w} and C_{D,α_w}. Without conducting wind tunnel experiments, these derivatives can only be obtained by differentiating the corresponding polars gained from the Montgomery approximation with respect to the angle of attack. Since the extrapolated polars of C_L and C_D are subject to uncertainties, so too are the derivatives C_{L,α_w} and C_{D,α_w}. However, the absolute changes in lift and drag $dL/d\alpha_w$ and $dD/d\alpha_w$ are quadratically proportional to the airspeed and significant control effectivities are only achieved at higher airspeeds, which are accompanied with smaller angles of attack and thus smaller errors in the polars.

To describe the change in the aerodynamic forces between two controller time steps more precisely, their dependency on a change in airspeed also needs to be considered. Since the airspeed is no direct function of the control variables, the derivative of the aerodynamic force with respect to the control variables can not be described. However, the inflow velocity is assumed to change slowly between two controller time steps and the induced change in aerodynamic force is considered negligible in context of the timescale separation. Taking all described aerodynamic effects into account, the aerodynamic related effectivity matrix $B_{A,h}$ is yielded, see A.2. The entire control effectivity matrix B can then be summed up according to Equation 18.

$$B = B_{G,h} + B_{T,h} + B_{A,h} \tag{18}$$

3.3 Attitude Controller

The attitude controller cascade, see Figure 6, is based on a rotational INDI controller described in [11, 13, 14], which determines the control inputs of the aircraft's main motors $\delta_{right}, \delta_{left}$, tail motor δ_{tail}, ailerons ξ and elevator η based on the control deviation in angular acceleration. The transfer function of the rotational INDI is approximated with the dynamic model of the aircraft's control devices. This allows for the use of a linear quadratic regulator (LQR) to calculate the optimal commanded angular accelerations based on the control deviation in thrust and attitude angles. Due to the coupling of attitude angles and the translational controller described in 3.2, the attitude control behaviour, analysed in [13], is included in the interpretation of the simulation results.

4 SIMULATION

The simulation is implemented in MATLAB/Simulink according to the dynamic model described in Section 2.1. The response to commanded velocity steps of $\pm 1\,\mathrm{m/s}$ in all translational axes is analyzed in both thrust- and wing-borne flight to verify the controller. The control performance in a velocity range of $0 - 8\,\mathrm{m/s}$ is also examined to account for the aircraft's ability to transition from thrust to wing-borne flight. In all cases, the translatory accelerations are limited to $\pm 1\,\mathrm{m/s^2}$, and all velocity steps are applied separately in all axes. The heading of the aircraft is kept constant for all simulations.

4.1 *Thrust-borne flight*

Figure 9 shows the step response of the velocity controller in thrust-borne flight. A similar response behavior can be observed in all axes, with a rise time of about $1.3\,s$ for both acceleration and deceleration with no noticeable overshoot. The response is slightly delayed at the beginning of the steps, resulting from *Idefix's* mass inertia and actuator dynamic.

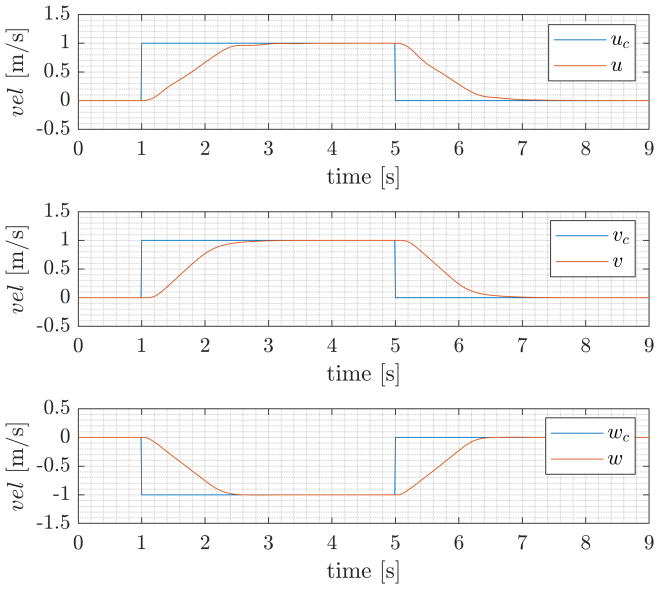

Figure 9: Velocity steps in thrust-borne flight ($0\,\mathrm{m/s}$)

This behavior can observed more clearly in the response behavior of the corresponding accelerations in Figure 10. It can also be seen, that the delay in y_h-direction is about $0.1\,\mathrm{s}$ more than in x_h- and z_h-direction. Since an acceleration in y_h-direction can only be indirectly achieved by a change in roll angle, this dynamic is significantly slower than accelerations in x_h- and z_h-direction, which are directly controlled of the control devices main motor thrust and tilt angle. It is also noticeable, that the commanded maximum acceleration is not reached in the time-span of the maneuver. This can be explained by the change of drag force induced by the change in velocity, which was neglected in the controller design due to the argumentation in Section 3. However, neglecting this effect has only a minor impact on the acceleration response behavior and does not significantly affect the control performance.

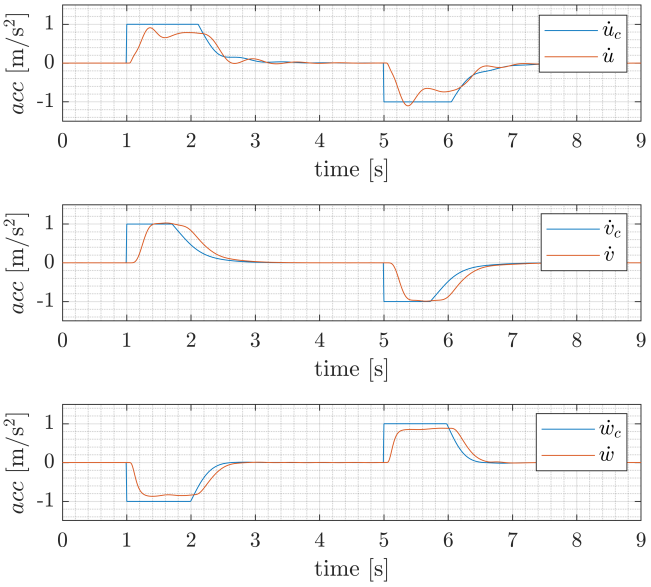

Figure 10: Accelerations in thrust-borne flight ($0\,\mathrm{m/s}$)

4.2 *Wing-borne flight*

In wing-borne flight, the velocity controller's step response shows similar behavior to that of the thrust-borne flight, see Figure 11.

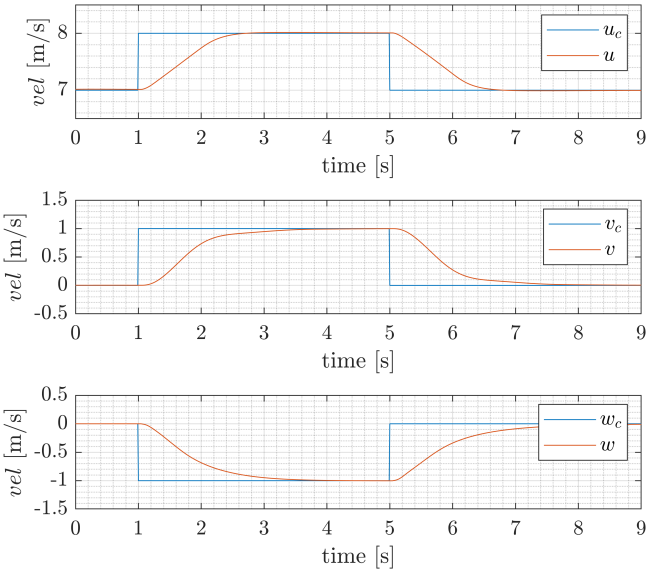

Figure 11: Velocity steps in wing-borne flight ($7\,\mathrm{m/s}$)

The only noticeable difference is a slightly longer rise time of about $1.5 - 2\,\mathrm{s}$. This effect can consequently be observed in the corresponding acceleration response, see Figure 12. The change in dynamic can be explained by the resistance increasing quadratically with airspeed and the change of the control variable responsible for the movement in y_h- and z_h-direction.

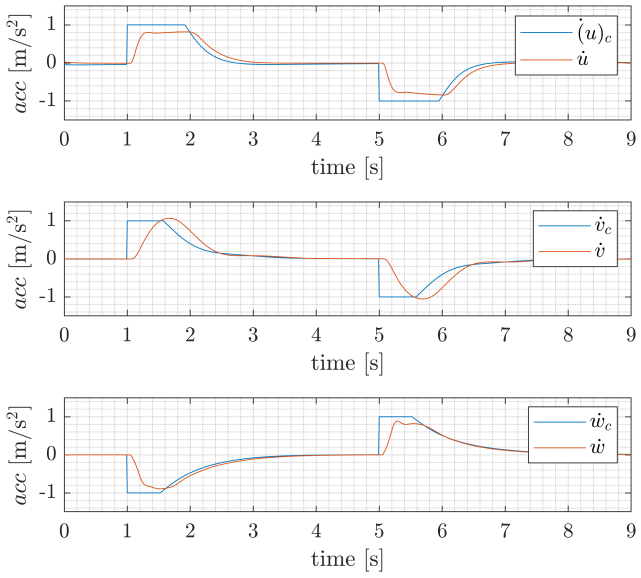

Figure 12: Acceleration in wing-borne flight ($7\,\mathrm{m/s}$)

Whereas in thrust-borne flight, the main motor was directly responsible for acceleration in z_h-direction, in wing-borne flight this is taken over by the change in pitch angle, which primarily changes the aircraft's attitude and subsequently the vertical acceleration. In y_h-direction, the acceleration is still induced by a change in roll angle, but the control device on attitude controller level changes from differential thrust to aileron deflection [11]. Even though these control devices have a similar dynamic, the roll damping in wing-borne flight is quadratically proportional to the airspeed [15] and therefore much higher than in thrust-borne flight. Since the control performance on velocity controller level is still sufficient, the assumptions made in the attitude controller and Chapter 3 can be considered valid.

4.3 Transition from thrust- to wing-borne flight

The control performance of the controller during the transition from thrust- to wing-borne flight is shown in Figure 13. During the transition, a steady increase in velocity at about $1\,\mathrm{m/s}$ can be observed with no noticeable influence on the velocities in y_h- and z_h-direction. This confirms the applicability of the translational INDI controller to the entire velocity range of the highly unsteady transition from thrust- to wing-borne flight.

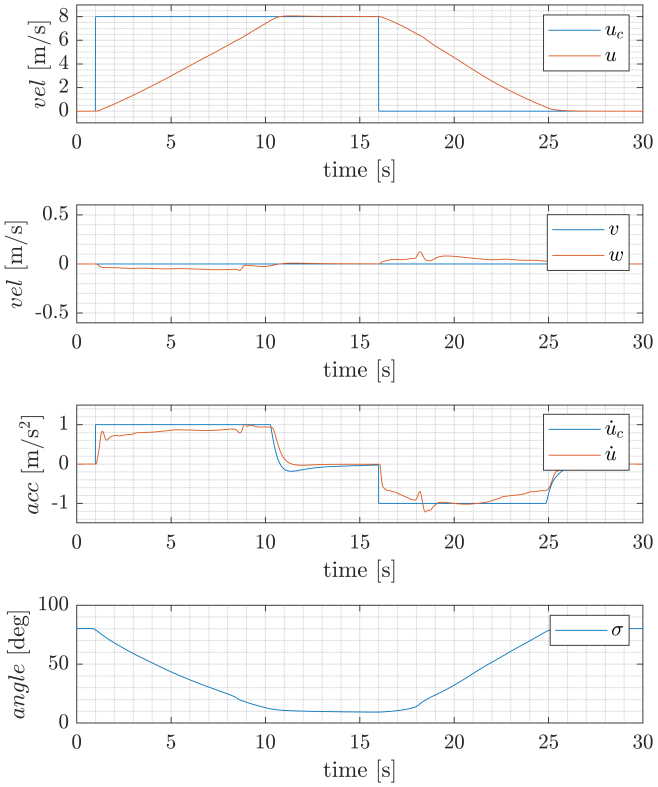

Figure 13: Transition from $0 - 8\,\mathrm{m/s}$

5 CONCLUSION

In this paper, a concept for operating a miniaturized tiltwing aircraft in confined spaces was presented. Taking into account tiltwing-specific flight dynamic constraints and a maximum longitudinal acceleration of $\pm 1\,\mathrm{m/s^2}$, it was shown, that an operation area $17\,\mathrm{x}\,17\,\mathrm{m}$ is sufficient for a full transition from thrust- to wing-borne flight along a circular path. Due to the absence of GNSS signals within enclosed spaces, an alternative concept based on ultrasound was employed to determine the aircraft's position and heading with an accuracy of $\pm 0.02\,\mathrm{m}$ and $\pm 2°$.

For the aircraft's translational control, a cascaded INDI based approach was implemented, showing complex interrelations between control variables and control effectivities. To improve the model of the control effectivities, in-flight measured aerodynamic forces were used in addition to standard lift and drag models. The functionality of the controller was validated in simulations with focus on the translational cascade. On velocity and acceleration level a stable and agile response behavior was achieved for thrust-born and wing-borne flight as well as the transition between both.

Future work will focus on translating this simulative work into fully autonomous real flights. Along with the controller

implementation of a circular transition pattern at a fixed height, this also includes a validation of the selected indoor navigation system and the integration in the existing navigation solution.

REFERENCES

[1] B. Montgomerie. Methods of Root Effects, Tip Effects and Extending the Angle of Attack Range to +- 180°, with Application to Aerodynamics for Blades on Wind Turbines and Propellers. *Swedish Defence Research Agency*, 2004.

[2] P. Hartmann. Vorausschauende Flugbahnregelung fuer Kippfluegelflugzeuge. 2017.

[3] I. Barz. Flugbahnplanung für Kippflügelflugzeuge zur Unterstützung im Rettungseinsatz. 2023.

[4] OptiTrack. `https://optitrack.com/`. Accessed: 2023-05-01.

[5] A. Masiero, F. Fissore, R. Antonello, A. Cenedese, and A. Vettore. A comparison of UWB and motion capture uav indoor positioning. *International Archives of the Photogrammetry, Remote Sensing and Spatial Information Sciences - ISPRS Archives*, 42(2/W13):1695–1699, 2019.

[6] Marvelmind Robotics. Ultrasonic positioning system `https://marvelmind.com/`. Accessed: 2023-05-01.

[7] J. Wendel. *Integrierte Navigationssysteme: Sensordatenfusion, GPS und Inertiale Navigation*. De Gruyter, 2011.

[8] Justin Winslow, Hikaru Otsuka, Bharath Govindarajan, and Inderjit Chopra. Basic understanding of airfoil characteristics at low reynolds numbers (10 4–10 5). *Journal of aircraft*, 55(3):1050–1061, 2018.

[9] Airfoil Tools. `http://airfoiltools.com/airfoil/details?airfoil=naca4415-il#polars`. Accessed: 2023-05-01.

[10] E. J.J. Smeur, G. C.H.E. de Croon, and Q. Chu. Cascaded incremental nonlinear dynamic inversion for MAV disturbance rejection. *Control Engineering Practice*, 73:79–90, 2018.

[11] Fabian Binz. Robust, Fault-Tolerant Control of Aircraft with Hovering Capability, 2020. Aachen.

[12] F. Binz T.Islam, D. Moormann. Attitude Control of Tiltwing Aircraft Using a Wing-Fixed Coordinate System and Incremental Nonlinear Dynamic Inversion. In *IEEE International Micro air vehicle conference and competition (IMAV)*, 2018.

[13] J. Müller D. Moormann. Miniaturization and Control of an Unmanned Tiltwing Aircraft. In *IEEE International Micro air vehicle conference and competition (IMAV)*, 2022.

[14] D. Schatten D. Moormann. Attitude control for a tiltwing aircraft under tail actuator failures. In *IEEE International Micro air vehicle conference and competition (IMAV)*, 2022.

[15] F. Binz D. Moormann. Actuator Modeling for Attitude Control Using Incremental Nonlinear Dynamic Inversion. In *IEEE International Micro air vehicle conference and competition (IMAV)*, 2019.

APPENDIX A: DATA

A.1 Thrust control effectivity

$$B_{T,h} = \begin{bmatrix} t_m\lambda_1 & -t_m\lambda_7 & -t\lambda_8 & \frac{dt_m}{d\delta_t}\lambda_6 \\ t_m\lambda_2 & 0 & t\lambda_4 & \frac{dt_m}{d\delta_t}\lambda_5 \\ t_m\lambda_3 & -t_m\lambda_6 & t\lambda_9 & -\frac{dt_m}{d\delta_t}\lambda_7 \end{bmatrix} \tag{19}$$

columns: $\phi, \theta, \sigma, t_m$
rows: $\dot{u}, \dot{v}, \dot{w}$

where:

$$\begin{aligned}
\lambda_1 &= \sin(\phi)\sin(\sigma)\sin(\theta) \\
\lambda_2 &= \cos(\phi)\sin(\sigma) \\
\lambda_3 &= \cos(\phi)\sin(\sigma)\sin(\theta) \\
\lambda_4 &= \cos(\sigma)\sin(\phi) \\
\lambda_5 &= \sin(\phi)\sin(\sigma) \\
\lambda_6 &= \cos(\theta)\cos(\sigma) - \cos(\phi)\sin(\theta)\sin(\sigma) \\
\lambda_7 &= \sin(\theta)\cos(\sigma) + \cos(\phi)\cos(\theta)\sin(\sigma) \\
\lambda_8 &= \cos(\theta)\sin(\sigma) + \cos(\phi)\sin(\theta)\cos(\sigma) \\
\lambda_9 &= \sin(\theta)\sin(\sigma) - \cos(\phi)\cos(\theta)\cos(\sigma)
\end{aligned}$$

A.2 Aerodynamic control effectivity

$$B_{A,h} = \begin{bmatrix} \left[\frac{d\vec{a}_{A,h}}{d\phi}\right]_x & \left[\frac{d\vec{a}_{A,h}}{d\theta}\right]_x & \left[\frac{d\vec{a}_{A,h}}{d\vec{\sigma}}\right]_x & 0 \\ \left[\frac{d\vec{a}_{A,h}}{d\phi}\right]_y & \left[\frac{d\vec{a}_{A,h}}{d\theta}\right]_y & \left[\frac{d\vec{a}_{A,h}}{d\vec{\sigma}}\right]_y & 0 \\ \left[\frac{d\vec{a}_{A,h}}{d\phi}\right]_z & \left[\frac{d\vec{a}_{A,h}}{d\theta}\right]_z & \left[\frac{d\vec{a}_{A,h}}{d\vec{\sigma}}\right]_z & 0 \end{bmatrix} \tag{20}$$

columns: $\phi, \theta, \sigma, t_m$
rows: $\dot{u}, \dot{v}, \dot{w}$

A.3 Angle of attack of the wing in horizontal coordinates

$$\alpha_{w,h} = \tan^{-1}\left(\frac{\sin(\gamma)\epsilon_1 \ + \epsilon_2\epsilon_3 - \epsilon_4}{\sin(\gamma)\epsilon_5 + \epsilon_2\epsilon_6 + \epsilon_7}\right) \tag{21}$$

where:

$$\begin{aligned}
\epsilon_1 &= \sin(\sigma)\sin(\theta) - \cos(\phi)\cos(\sigma)\cos(\theta) \\
\epsilon_2 &= \cos(\beta_f)\cos(\gamma) \\
\epsilon_3 &= \cos(\theta)\sin(\sigma) + \cos(\phi)\cos(\sigma)\sin(\theta) \\
\epsilon_4 &= \cos(\gamma)\sin(\beta_f)\cos(\sigma)\sin(\phi) \\
\epsilon_5 &= \cos(\sigma)\sin(\theta) + \cos(\phi)\cos(\theta)\sin(\sigma) \\
\epsilon_6 &= \cos(\sigma)\cos(\theta) - \cos(\phi)\sin(\sigma)\sin(\theta) \\
\epsilon_7 &= \cos(\gamma)\sin(\beta_f)\sin(\phi)\sin(\sigma)
\end{aligned} \tag{22}$$